Electronic Supplementary Information

Tailoring MMn_2O_4 Spinels Anchored on Nitrogen doped Reduced Graphene Oxide for High Performance Bifunctional Water Splitting

Madakannu Iyyappan,[a] Ayyavu Shankar,[a] Govindan Maduraiveeran*[a,b] and K. K. R. Datta*[a]

[a]Department of Chemistry, Faculty of Engineering and Technology, SRM Institute of Science and Technology, Kattankulathur – 603203, Tamil Nadu, India.

[b]Materials Research Center, American University of Sharjah, Sharjah, 26666, United Arab Emirates

**Corresponding Author:* mgovindhan@aus.edu & pgmadura@yahoo.co.in (GM) and kumarard@srmist.edu.in & kkrdatta@gmail.com (KKRD)

Materials characterization

The electrocatalysts were subjected to various analytical techniques for characterization. Fourier-transform infrared spectra (FT-IR) were recorded using an IR-Tracer 100 Shimadzu infrared spectrometer. Raman spectrum was recorded using HORIBA, LabRam HR Evolution. Powder X-ray diffraction (PXRD) measurements were conducted using a PANalytical X'pert3 powder X-ray diffractometer. Morphology studies were carried out with a FEI QUANTA 200 scanning electron microscope operating at a 20 kV accelerating voltage. Transmission electron microscopy (TEM) analyses of $FeMn_2O_4$@N-rGO were performed using a JEOL JEM-2100 plus microscope. X-ray photoelectron spectroscopy measurements were conducted utilizing a ULVAC-PHI, Inc. instrument, specifically the PHI5000 Version Probe III equipped with monochromatic Al Kα radiation ($h\nu = 1486.6$ eV). High-resolution spectra (Fe 2p, Co 2p, Cu 2p, Zn 2p, Mn 2p, O 1s, N 1s) were acquired at 20 eV pass energy and 50 ms dwell time with charge neutralization. Binding Energies were calibrated to adventitious C 1s (284.8 eV). Analysis used CasaXPS with linear background and GL(30) line shapes

Electrochemical characterization

The catalyst ink was prepared by dispersing 10 mg of the catalysts in the Nafion solution (10 µL) and isopropanol (490 µL). All electrochemical experiment tests were accomplished in a standard three-electrode cells using ORIGA Flex OGF500 model potentiostat at room temperature. In the three-electrode system, the reference electrode utilized was Ag/AgCl (3.0

KCl), the counter electrode consisted of a platinum coil, and the working electrode was the NF electrode (1cm^2) in an aqueous 1 M KOH solution at room temperature. All Electrode potentials were calibrated against the reversible hydrogen electrode (RHE) using E(RHE) = E(Ag/AgCl) + 1.016 V+ 0.0591 V × pH. In comparison, commercial RuO_2 and Pt/C, 10% modified NF (RuO_2@NF and Pt/C@NF) for OER and HER were prepared in the similar way. Cyclic voltammetric (CV) measurements were conducted at a sweep rate of 20 mV.s^{-1}, and the linear sweep voltammetry (LSV) measurements for OER and HER were recorded at a scan rate of 5 mV s^{-1} without iR compensation. All the measurements were performed in alkaline conditions (1 M KOH). The kinetics of the OER and HER processes were investigated from LSV data using the Tafel equation and Electrochemical Impedance Spectroscopy (EIS) in a frequency range spanning from 1 kHz to 100 MHz, with various applied potentials. Double-layer capacitance (C_{dl}) was estimated by CV at scan rates of 10, 20, 50, 75, and 100 mV s^{-1} in the non-Faradaic region. Overall water splitting performance was evaluated by assembling $FeMn_2O_4$@N-rGO || $FeMn_2O_4$@N-rGO, and commercial RuO_2||Pt/C couples act as both cathode and anode, respectively. The LSV curves of two electrode configurations were recorded at 5 mV s^{-1}, and chronoamperometry stability tests carried out at a current density of 10 mA·cm^{-2} for 10 h in 1 M KOH.

Calculation Methods

Turn over frequency (TOF) value was calculated based on the equation of

$$TOF = \frac{jS}{4Fm} \quad (1)$$

In the equation, j is the current density at a specific overpotential, S represents the electrode's geometric surface area, F means the Faraday constant, and m is the number of moles of metals on the electrode.

Tafel slope (b) was calculated from the polarisation curve data to the Tafel equation of a + b log |j|, where j is the current density at the specified overpotential and “a” and “b” are Tafel constants. “η” represents the overpotential for OER and HER.

Double-layer capacitance (C_{dl}) was determined from the slope of charging currents (i_c) as a function of scan rate (υ), as shown in Eqn. (2). This was done to determine the average absolute value of the cathodic and anodic slopes of the linear fitting of the plot.

$$i_c = \upsilon C_{dl} \quad (2)$$

Using eqn. (3), the electrochemically active surface area (ECSA) of $FeMn_2O_4$@N-rGO was calculated from the catalytic surface's electrochemical double-layer capacitance.

$$ECSA = \frac{C_{dl}}{Cs \times A} \quad (3)$$

C_{dl} is double-layer capacitance, A is the electrode area (1 cm^2 for our working electrodes) and Cs is the specific capacitance value of 1.0 M KOH (0.040 mF). The electrochemical double-layer capacitance for the $FeMn_2O_4$-N-rGO catalyst was C_{dl}=80 mF cm^2.

In detail, CVs were recorded in a 1.0 M alkaline KOH in a potential window of 0.7 to 1.6 V vs. RHE at a scan rate of 20 mV s^{-1}. Integrating the area under the voltage vs. current density gives the voltametric charge, which was used to determine the number of active sites in eqn. (4).

$$n = \frac{Q}{4F} \quad (4)$$

Where, "n" is the number of active sites (moles), "Q" is voltametric charge, "F" is the Faraday constant (96,480 C/mol), "4" is the number of electrons transferred during OER.

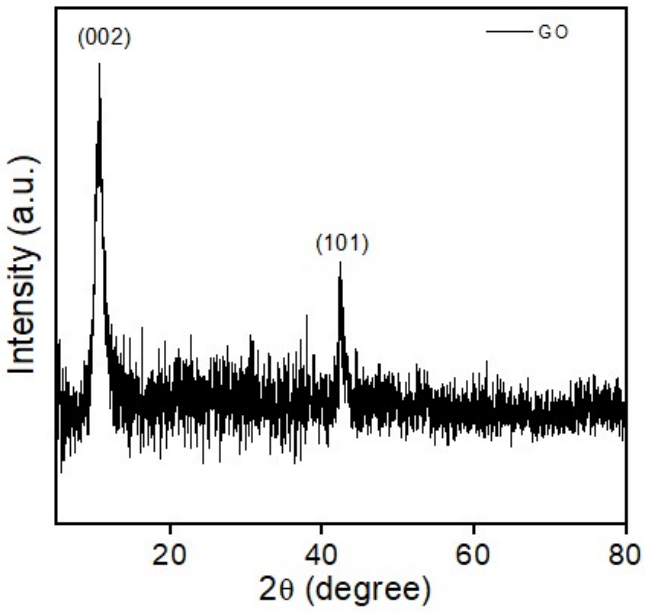

Fig. S1. PXRD pattern of graphene oxide (GO).

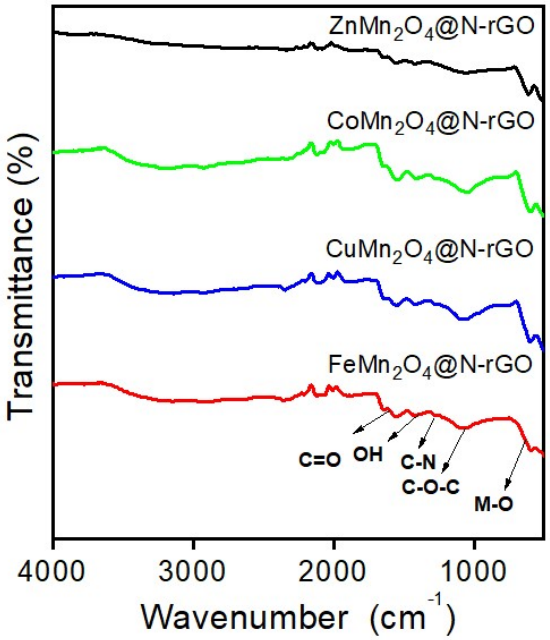

Fig. S2. FT-IR spectra of MMn_2O_4 oxides (M= Fe, Co, Cu and Zn) embedded over N-rGO.

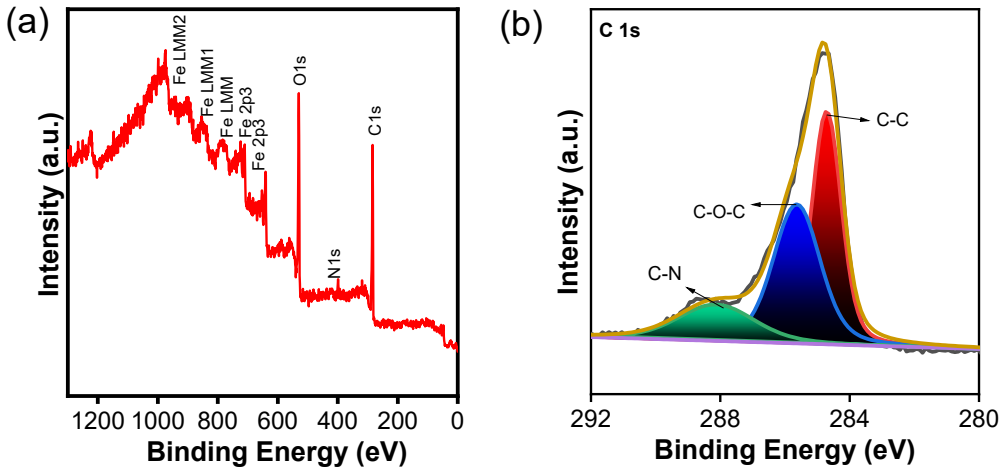

Fig. S3. (a) XP survey scan and (b) HR-XPS of C1s of $FeMn_2O_4$@N-rGO heterostructures.

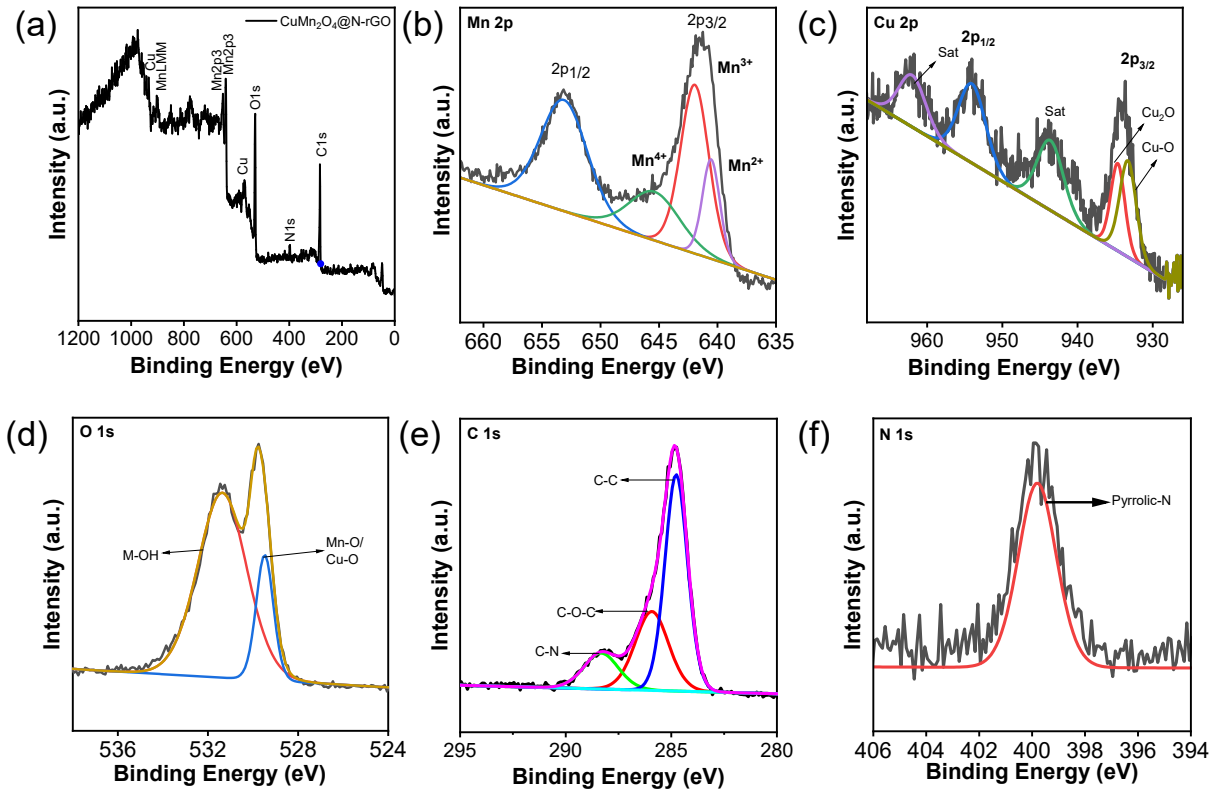

Fig. S4. High-resolution XP spectra (a) survey spectrum (b) Mn 2p (c) Cu 2p, (d) O 1s and (e) C1s and (f) N1s of $CuMn_2O_4$@N-rGO heterostructures.

The survey spectrum reveals the presence of Cu, Mn, O, N and C elements with atomic percentages of 1, 18.1, 31, 5 and 44.9 respectively (Fig. S4a). The deconvoluted high-resolution Cu 2p XPS (Fig. S4c) reveals that copper present in mixed oxidation states. The Cu $2p_{3/2}$ region shows two components at binding energies of 933.3 and 934.7 eV, which are assigned to Cu^{+} and Cu^{2+} along with the satellite peak at 943.5 eV is a characteristic feature of Cu^{2+}.[1-3] The Cu $2p_{1/2}$ peak appears at 954.2 eV, and the resulting spin–orbit splitting of approximately 20 eV is consistent with reported values for copper oxide systems. As shown in Fig. S4b, the deconvoluted peaks of Mn 2p XPS has B.E. of peaks at 640.37 eV assigned to Mn^{3+} and another at 642.1 eV corresponding to Mn^{4+} accompanied by satellite peak at 645.7 eV. The peak at 653.02 eV corresponds to $Mn2p_{1/2}$. In the O 1s XP spectrum deconvoluted into two peaks at 529.4 eV corresponds to lattice oxygen (Cu-O/Mn-O) and 531.3 eV corresponds to metal hydroxyl groups as shown in Fig. S4d. The C 1s XP spectrum (Fig. S4e) can be deconvoluted into three peaks at 284.7, 285.9, and 288.2 eV, corresponding to graphitic carbon (C–C), C–O, and C-N, respectively. Furthermore, as shown Fig. S4f, N1s spectrum a peak at 399.7 eV corresponds to pyrrolic N, similar to that of nitrogen-doped rGO networks.

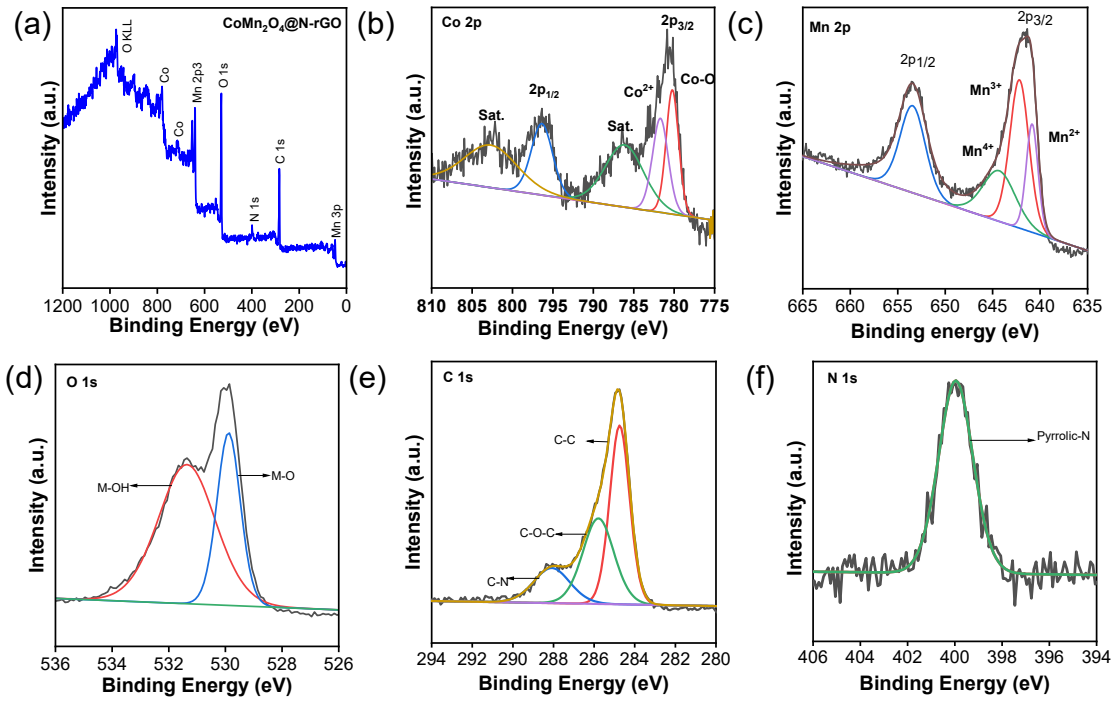

Fig. S5. High-resolution XP spectra (a) survey spectrum (b) Co 2p (c) Mn 2p, (d) O 1s and (e) C1s and (f) N1s of $CoMn_2O_4$-N-rGO heterostructures.

The survey spectrum reveals the presence of Co, Mn, O, N and C elements with atomic percentages of 9.6, 13.7, 31.2, 4.0 and 41.5 respectively (Fig. S5a). The high-resolution Co 2p XPS (Fig. S5b) spectrum of $CoMn_2O_4$ reveals the coexistence of mixed cobalt oxidation states. The Co $2p_{3/2}$ has deconvoluted into two BE peaks at 780.4 and 781.7 eV, which are assigned to Co^{3+} and Co^{2+}. The presence of an intense shake-up satellite at 786.4 eV characteristic feature of cobalt in +2 oxidation state.[4, 5] The BE at 796.31 eV corresponding Co $2p_{1/2}$ along with a satellite feature at 802.54 eV. As shown in Fig. S5c, the deconvoluted peaks of Mn 2p have BE of peaks at 640.06 eV assigned to Mn^{3+} and another at 642.1 eV corresponding to Mn^{4+} accompanied by satellite peak at 644.2 eV. The peak at 653.22 corresponds to $Mn2p_{1/2}$. In the O 1s XPS spectrum deconvoluted into two peaks at 529.88 eV corresponds to lattice oxygen (Co-O/Mn-O) and 531.2 eV corresponds to hydroxyl groups as shown in Fig. S5d. The C 1s XP spectrum (Fig. S5e) can be deconvoluted into three peaks at 284.7, 285.7, and 288.1 eV, corresponding to graphitic carbon (C–C), C–O, and C-N, respectively. Furthermore, as shown Fig. S5f, N1s spectrum a peak at 399 eV corresponding to pyrrolic N.

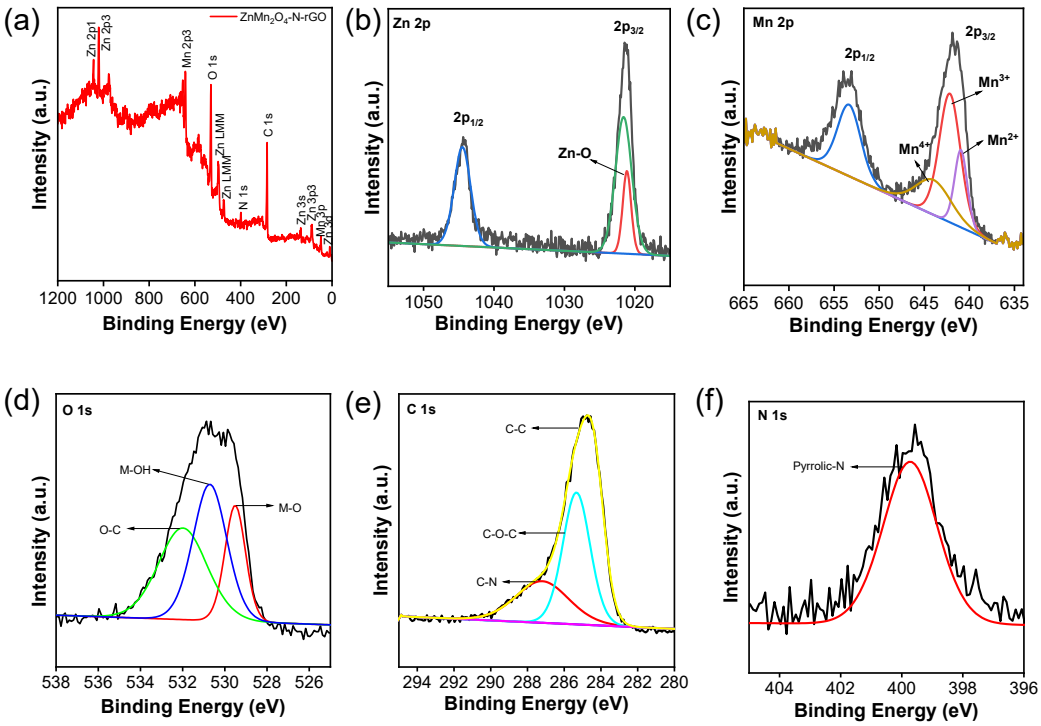

Fig. S6. High-resolution XP spectra (a) survey spectrum (b) Zn 2p (c) Mn 2p, (d) O 1s (e) C1s and (f) N1s of $ZnMn_2O_4$-N-rGO heterostructures.

The survey spectrum reveals the presence of Zn, Mn, O, N and C elements with atomic percentages of 3.3, 11.9, 28.8, 3.39 and 52 respectively (Fig. S6a). The high-resolution Zn 2p XP spectrum (Fig. S6b) of the $ZnMn_2O_4$ sample can be deconvoluted into three binding energies at 1020.52, 1021.23 eV corresponding to Zn^{2+} species of Zn $2p_{3/2}$ and 1044.50 eV the spin–orbit splitting between the Zn $2p_{3/2}$ and Zn $2p_{1/2}$ levels (~23.3 eV) is consistent with reported values for Zn^{2+} in zinc-based oxide.[6, 7] As shown in Fig. S6c the main Mn $2p_{3/2}$ peak at 640.8 eV corresponds to Mn^{3+} while the peak at 642.16 eV corresponds to Mn^{4+}. In addition, a satellite peak at feature at 644.50 eV is associated with Mn^{3+} species. In the O 1s XPS (Fig. S6d) deconvoluted into two peaks at 529.46 eV corresponds to lattice oxygen (Zn-O / Mn-O) and 530.73 eV corresponds to hydroxyl groups and 532 eV corresponds to oxygen network from rGO functionalities. The C 1s XP spectrum (Fig. S6e) can be deconvoluted into three peaks at 284.7, 285.7, and 288.1 eV, corresponding to graphitic carbon (C–C), C–O, and C-N, respectively. Furthermore, as shown Fig. S6f, N1s spectrum a peak at 399 eV corresponds to pyrrolic N respectively.

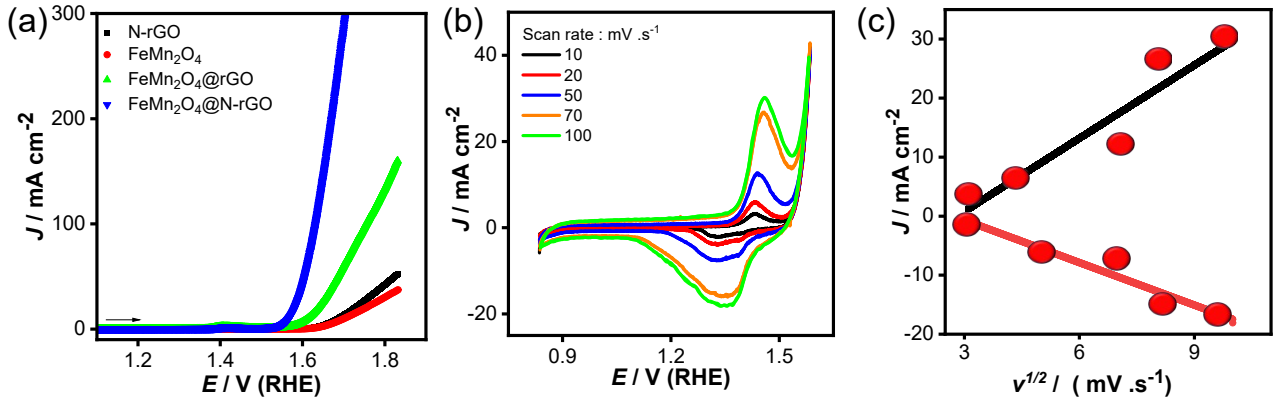

Fig. S7. Electrochemical characterization of $FeMn_2O_4$@N-rGO in 1 M KOH: (a) LSV comparison with $FeMn_2O_4$ and N-rGO, (b) CVs at scan rates of 10–100 mV s^{-1}; and (c) capacitive current plotted against the square root of scan rate.

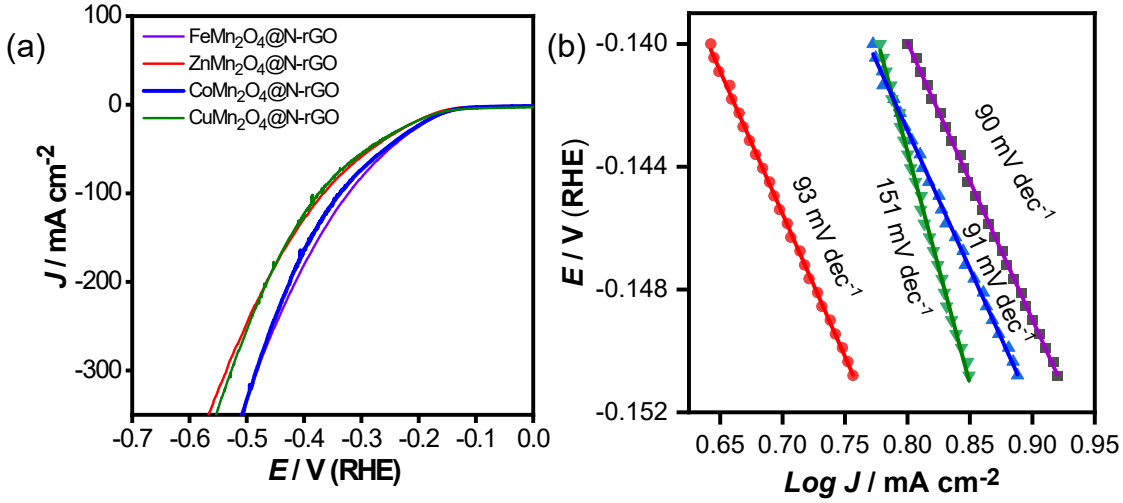

Fig. S8. (a) HER polarization curves of MMn_2O_4 (M = Fe, Co, Cu, and Zn) oxides embedded on N-rGO in 1 M KOH. (b) Corresponding Tafel plots of the catalysts.

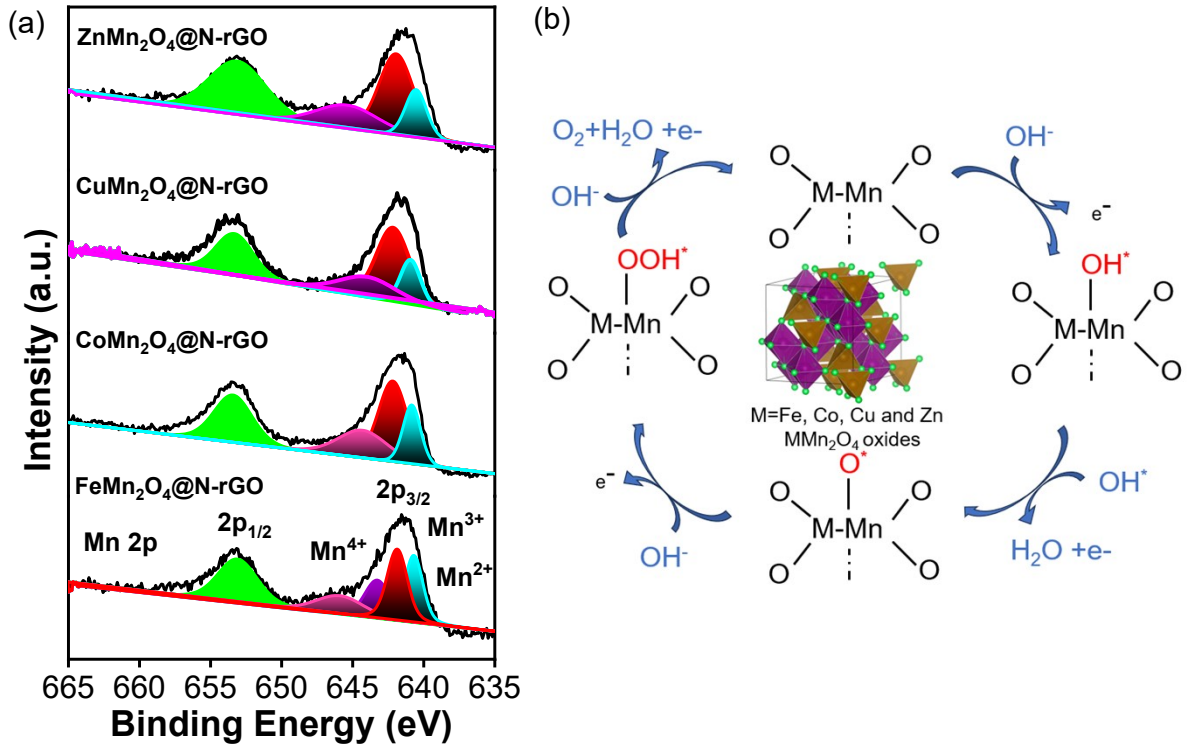

Fig. S9. (a) High resolution Mn 2p XP spectra overlap of various MMn_2O_4 oxides (M= Fe, Co, Cu and Zn) embedded over N-rGO (b) Proposed Mechanism of OER in 1 M KOH.

The electronic structure and oxidation states of Mn in MMn_2O_4-N-rGO were investigated through high-resolution Mn 2p XP spectra (Fig. S9a). The deconvolution of the Mn $2p_{3/2}$ and Mn $2p_{1/2}$ peaks reveal the coexistence of Mn^{2+}, Mn^{3+} and Mn^{4+} oxidation states, with Mn^{3+} being the predominant species.[8, 9] . The proposed mechanism (Fig. S9b) underscores the role of Mn–O bond symmetry and electron redistribution enabling a favourable pathway for oxygen evolution[10, 11]. This adsorption is facilitated by the presence of active sites on the catalyst surface, which may be due to bimetallic oxide cations and nitrogen doped rGO matrix. Upon adsorption, the hydroxyl groups in rGO facilitated electron transfer process. This transfer of electrons from the catalyst to the adsorbed species initiates their activation, leading to the formation of reactive intermediates. The activated oxygen moieties in rGO further transforms into oxo species (-O-) through chemical rearrangements on the catalyst surface. Subsequently, the oxo species further react with hydroxyl groups forming oxo-hydroxo species (-OOH). These intermediates are key species in the oxygen evolution reaction pathway and in the final step, the oxo-hydroxo species under rGO dissociation leading to the evolution of molecular oxygen (O_2). We expect throughout the mechanism, the presence of $FeMn_2O_4$ as the active

component supported on N-doped rGO providing catalytic sites for the various OER steps. The N-doped rGO matrix enhances the conductivity and stability of the catalyst, while also contributing to the adsorption and activation of hydroxyl ion [12-14] .

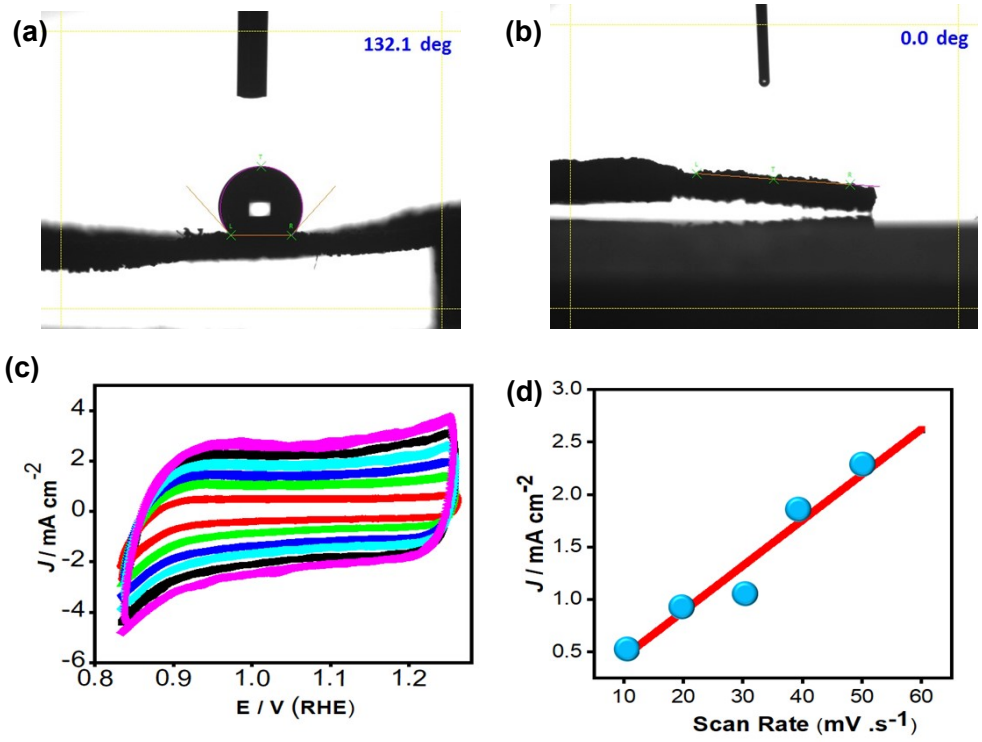

Fig. S10. Water contact angle measurements of the (a) bare NF and (b) $FeMn_2O_4$@N-rGO electrodes (c and d) ECSA measurement in non-faradic region of $FeMn_2O_4$@N-rGO heterostructures.

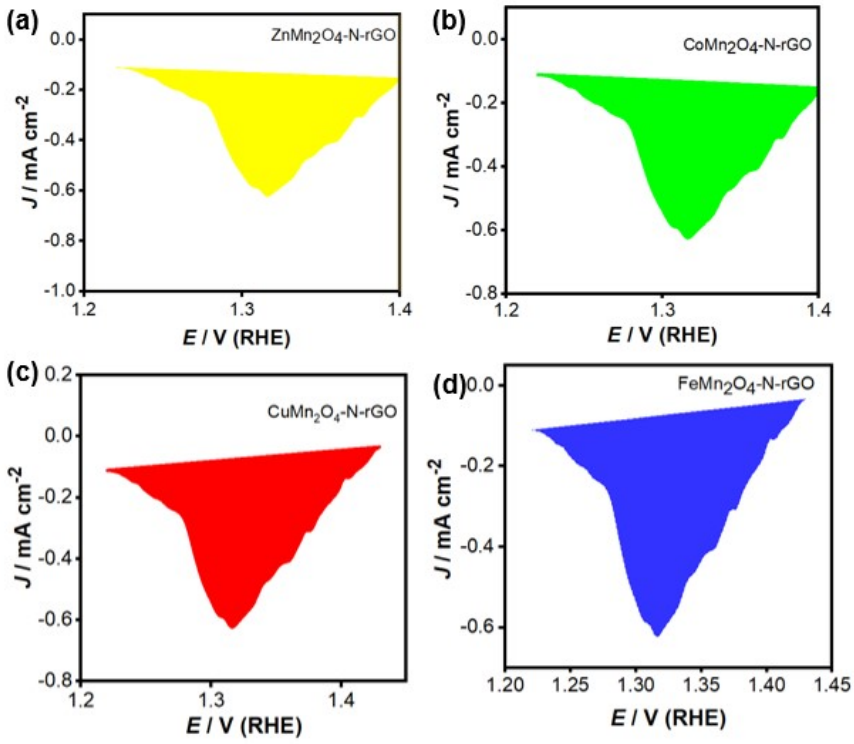

Fig. S11. Isolated cathodic (reduction) peaks extracted from the CV curves and used for charge integration to estimate the number of electrochemically active sites for (a) $ZnMn_2O_4$@N-rGO, (b) $CoMn_2O_4$@N-rGO, (c) $CuMn_2O_4$@N-rGO, and (d) $FeMn_2O_4$@N-rGO heterostructure electrodes.

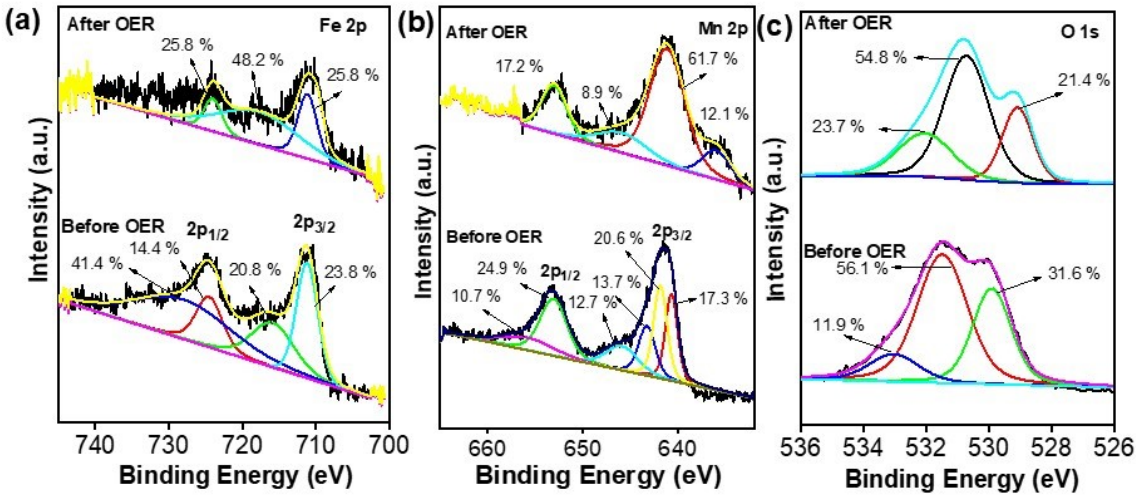

Fig. S12. HR-XPS of (a) Fe 2p, (b) Mn 2p and (c) O1s after and before OER stability of the $FeMn_2O_4$@N-rGO heterostructures.

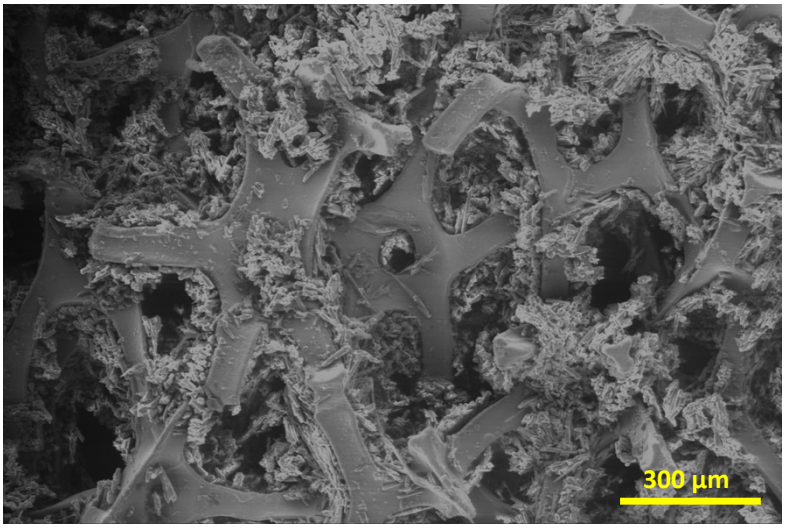

Fig. S13. Post FE-SEM analysis of the $FeMn_2O_4$@N-rGO heterostructures after 50 h of durability test

Table S1. Summary of OER activity metrics, including onset potential, overpotential, Tafel slope, turnover frequency, and active site density for the as-prepared electrocatalysts.

Sample	**Onset Potential V vs RHE**	**Overpotential @10 mA cm^{-2} (mV)**	**Maximum current density mA cm^{-2}**	**Tafel Value mV dec^{-1}**	**Turnover frequency (TOF) s^{-1}**	**Number of Active Sites mole**
$CoMn_2O_4$-N-rGO	1.58	390	212	97	1.0	0.05
$CuMn_2O_4$-N-rGO	1.57	440	383	187	1.1	0.06
$ZnMn_2O_4$-N-rGO	1.59	400	151	122	0.6	0.04
$FeMn_2O_4$-N-rGO	1.50	330	558	90	3	0.14

Table S2. Comparative OER performance of $FeMn_2O_4$-N-rGO heterostructures electrode and previously reported binary and ternary spinel catalysts prepared using various synthesis routes.

Sl. No.	Catalyst	Synthesis method	Electrode	η OER	Ref.
1	FeMn oxides/Ni Foam ($Fe_xMn_{3-x}O_4$)	Solvothermal 120 °C for 12 h Annealing 350°C for 2 h	NF	η_{10} = 258 mV Tafel Value: 28.7 mV·dec^{-1}	15
2	$Fe_{12}Ni_{23}Cr_{10}Co_{55-x}Mn_x$/CNT	Heating 120 °C for 3 h sintered at 900 °C for 2 h in (Ar mixed with 10% H_2)	NF	η_{10} =0.7 V Tafel Value: 250 mV dec^{-1}	16
3	Co−Fe−Cr−Mo Spinel/NF Foam	Hydrothermal 120 °C for 12 h Dried at 120 °C for 12 h	NF	η_{10} = 196 mV Tafel Value: 33 mV dec^{-1}	17
4	$FeMn_2O_4$-Q	Quenching 500 ^{O}C-3 h	CC	η_{10} = 350 mV Tafel Value: 100.7 mV dec^{-1}	18
5	m-$MnCo_2O_4$	Spin coating followed by annealing at 250 to 700^{o} C for 1 h	RDE	η_{10} = 300 mV 85 mV dec^{-1}	19
6	$Mn_xCo_{3-x}O_4$	Calcined at 600 ^{o} C	NF	η_{10} = 345 mV 74.3 mV dec^{-1}	20
7	$MnFe_2O_4$@C	Solvothermal for 180 ^{o} C for 12 h again 180 ^{o} C for 12 h followed by 650 180 ^{o} C for 2 h in Ar last 350 ^{o} C for 2 h in air	RDE	η_{10} =370 mV 95 mV dec^{-1}	21
8	$MnCo_2O_4$-rGO	Hydrothermal 200 °C for 6 h followed by annealing at 600 °C for 3 h	RDE	Onset : 1.56 V η_{10} = NM 106.9 mV dec^{-1}	22
9	Ce- $MnCo_2O_4$	Annealing at 500 °C for 4 h	GCE	η_{10} =390 mV 125 mV dec^{-1}	23
10	$FeMn_2O_4$-N-rGO	Solvothermal 120 °C for 3 h	NF	η_{10} =330 mV 90 mV dec^{-1}	This work

References

1. P. Suresh, S. P. Muthu, A. Kumar, M. Ubaidullah and A. Natarajan, *Journal of Environmental Chemical Engineering*, 2025, **13**, 119912.
2. B. J. Rani, A. Sivanantham, T. S. Shridharan, T. Runfa and I. S. Cho, *Journal of Materials Chemistry A*, 2022, **10**, 17710-17720.
3. I. Madakannu, I. Patil, B. Kakade and K. K. R. Datta, *Beilstein Journal of Nanotechnology*, 2022, **13**, 1020-1029.
4. M. Krishnamachari, M. Kumar, M. S. Pandian and J.-H. Chang, *Nanoscale*, 2025, **17**, 18190-18201.
5. J. Lee, N. Son, N.-K. Park, H.-J. Ryu, J.-I. Baek, Y. Sohn, J. Y. Do and M. Kang, *Electrochimica Acta*, 2021, **379**, 138168.
6. S. Sekar, S. Sadhasivam, A. Shanmugam, S. Saravanan, I. Pugazhendi, Y. Lee, D. Y. Kim, R. Manikandan, S.-C. Chang and S. Lee, *International Journal of Hydrogen Energy*, 2025, **141**, 721-728.
7. S. Aman, N. Ahmad, S. Manzoor, M. M. Alanazi, S. A. M. Abdelmohsen, R. Y. Khosa, A. G. Al-Sehemi, R. Hua, H. A. Alzahrani and A. H. Chughtai, *Catalysis Surveys from Asia*, 2023, **27**, 165-179.
8. H. Feizi, S. M. Hosseini, Z. Zand and M. M. Najafpour, *International Journal of Hydrogen Energy*, 2022, **47**, 7813-7822.
9. V. Celorrio, A. S. Leach, H. Huang, S. Hayama, A. Freeman, D. W. Inwood, D. J. Fermin and A. E. Russell, *ACS Catalysis*, 2021, **11**, 6431-6439.
10. P. Wang, S. Zhang, Z. Wang, Y. Mo, X. Luo, F. Yang, M. Lv, Z. Li and X. Liu, *Journal of Materials Chemistry A*, 2023, **11**, 5476-5494.
11. H. Radinger, P. Connor, R. Stark, W. Jaegermann and B. Kaiser, *ChemCatChem*, 2021, **13**, 1175-1185.
12. Y. Xue, Y. Wang, Z. Zheng, Q. Lu, W. Chen, S. Yan, S. Sun, H. Zhang and G. Shao, *Journal of Electroanalytical Chemistry*, 2024, **963**, 118329.
13. M. Guo, R. Deng, C. Wang and Q. Zhang, *Journal of Energy Chemistry*, 2023, **78**, 537-553.
14. Y. Li, H. Shen, B. Zhou, J. Li, L. Wang, Q. Sun, S. Ramakrishna, M. Luo, D. Ji and X. Qin, *Matter*, 2024, **7**, 1245-1258.
15. Y. Yuan, Z. Jiang, M. Li and K. Peng, *ACS Applied Energy Materials*, 2023, **6**, 7865-7876.
16. X. Cao, Y. Gao, Z. Wang, H. Zeng, Y. Song, S. Tang, L. Luo and S. Gong, *ACS Applied Materials & Interfaces*, 2023, **15**, 32365-32375.
17. H. Pang, T. Gao, W. Zhao, L. Liu, E. Liu, H. Wen and T. Sun, *Fuel*, 2024, **374**, 132532.
18. C. Qi, Q. Liu, Y. Dong, G. Zhang, X. Jiang and D. Gao, *Journal of Alloys and Compounds*, 2023, **967**, 171754.
19. A. Amirzhanova, N. Akmanşen, I. Karakaya and Ö. Dag, *ACS Applied Energy Materials*, 2021, **4**, 2769-2785.
20. K. Lankauf, K. Cysewska, J. Karczewski, A. Mielewczyk-Gryń, K. Górnicka, G. Cempura, M. Chen, P. Jasiński and S. Molin, *International Journal of Hydrogen Energy*, 2020, **45**, 14867-14879.
21. Z. Zhang, D. Zhou, S. Zou, X. Bao and X. He, *Journal of Alloys and Compounds*, 2019, **786**, 565-569.
22. H. Yang, M. Zhu, X. Guo, C. Yan and S. Lin, *ACS Omega*, 2019, **4**, 22325-22331.
23. X. Huang, H. Zheng, G. Lu, P. Wang, L. Xing, J. Wang and G. Wang, *ACS Sustainable Chemistry & Engineering*, 2019, **7**, 1169-1177.